



1 **Estimating global surface ammonia concentrations inferred**
2 **from satellite retrievals**

3

4 Lei Liu ^{a,b}, Xiuying Zhang ^{a,*}, Anthony Y.H. Wong ^b, Wen Xu ^c, Xuejun Liu ^c, Yi Li ^d,

5 Huan Mi ^{e,b}, Xuehe Lu ^a, Limin Zhao ^a, Zhen Wang ^a, Xiaodi Wu ^{a,f}

6

7 ^a International Institute for Earth System Science, Nanjing University, Nanjing,

8 210023, China

9 ^b Department of Earth and Environment, Boston University, Boston, Massachusetts,

10 USA

11 ^c College of Resources and Environmental Sciences, Centre for Resources,

12 Environment and Food Security, Key Lab of Plant-Soil Interactions of MOE, China

13 Agricultural University, Beijing, 100193, China

14 ^d Sunset CES Inc., Beaverton, OR, 97008, USA

15 ^e College of Surveying and Geo-Informatics, Tongji University, 1239 Siping Road,

16 Shanghai, China

17 ^f Jiangsu Center for Collaborative Innovation in Geographical Information Resource

18 Development and Application, Nanjing, 210023, China

19 * Correspondence to Xiuying Zhang (zhangxy@nju.edu.cn).

20

21 **Abstract**

22 Ammonia (NH₃), as an alkaline gas in the atmosphere, can cause direct or indirect
23 effects on the air quality, soil acidification, climate change as well as human health.

24 Estimating surface NH₃ concentrations is critically important for modelling the dry
25 deposition of NH₃, which has important impacts on the natural environment. However,
26 sparse monitoring sites make it challenging and difficult to understand the global
27 distribution of surface NH₃ concentrations both in time and space. We estimated the
28 global surface NH₃ concentrations for the years of 2008-2016 using the satellite NH₃
29 retrievals combining its vertical profiles from the GEOS-Chem. The accuracy



30 assessment indicates that the satellite-based approach has achieved a high predictive
31 power for annual surface NH_3 concentrations compared with the measurements of all
32 sites in China, US and Europe ($R^2=0.76$ and $\text{RMSE}=1.50 \mu\text{g N m}^{-3}$). The
33 satellite-derived surface NH_3 concentrations had higher consistency with the
34 ground-based measurements in China ($R^2=0.71$ and $\text{RMSE}=2.6 \mu\text{g N m}^{-3}$) than the US
35 ($R^2=0.45$ and $\text{RMSE}=0.76 \mu\text{g N m}^{-3}$) and Europe ($R^2=0.45$ and $\text{RMSE}=0.86 \mu\text{g N m}^{-3}$)
36 at a yearly scale. Annual surface NH_3 concentrations higher than $6 \mu\text{g N m}^{-3}$ are
37 mainly concentrated in the North China Plain of China and Northern India, followed
38 by $2\text{--}6 \mu\text{g N m}^{-3}$ mainly in southern and northeastern China, India, western Europe
39 and eastern United States (US). High surface NH_3 concentrations were found in the
40 croplands in China, US and Europe, and surface NH_3 concentrations in the croplands
41 in China were approximately double than those in the croplands in the US and Europe.
42 The linear trend analysis shows that an increase rate of surface NH_3 concentrations
43 ($>0.2 \mu\text{g N m}^{-3} \text{ y}^{-1}$) appeared in the eastern China during 2008–2016, and a middle
44 increase rate ($0.1\text{--}0.2 \mu\text{g N m}^{-3} \text{ y}^{-1}$) occurred in northern Xinjiang over China. NH_3
45 increase was also found in agricultural regions in middle and eastern US with an
46 annual increase rate of lower than $0.10 \mu\text{g N m}^{-3} \text{ y}^{-1}$. The satellite-derived surface NH_3
47 concentrations help us to determine the NH_3 pollution status in the areas without
48 monitoring sites and to estimate the dry deposition of NH_3 in the future.

49

50 **Introduction**

51 Ammonia (NH_3), emitted primarily by agricultural activities and biomass burning, is
52 an important alkaline gas in the atmosphere (Van Damme et al., 2018; Warner et al.,
53 2017). Excessive surface NH_3 concentrations can cause chronic or acute damage to
54 the plant (such as reduced growth and bleached gray foliage) when its capacity of
55 detoxification is exceeded (Eerden, 1982; Sheppard et al., 2008). Estimation of surface
56 NH_3 concentrations is critically important in modelling the dry deposition of NH_3 ,
57 which may comprise a large part of atmospheric nitrogen (N) deposition, and could
58 cause acidification in the soil, eutrophication in the aquatic ecosystems, and



59 contamination in drinking water (Basto et al., 2015; Kim et al., 2014; Lamarque et al.,
60 2005; Larssen et al., 2011; Reay et al., 2008). In addition, NH_3 can also react with
61 nitric acid and sulfuric acid to form ammonium salts (Li et al., 2014; Li et al., 2017b),
62 which are important components of particulate matters (PM), and have negative
63 impacts on air quality and human health (Xu et al., 2017; Schaap et al., 2004).

64

65 Several national monitoring programs have been established to quantify surface NH_3
66 concentrations, including the Chinese Nationwide Nitrogen Deposition Monitoring
67 Network (NNDMN) established in 2004, the Ammonia Monitoring Network in China
68 (AMoN-China) established in 2015 in China, the Ammonia Monitoring Network in
69 the US (AMoN-US) as well as the European Monitoring and Evaluation Programme
70 (EMEP). However, there are still relatively large uncertainties of estimating global
71 surface NH_3 concentrations, resulting from the sparse monitoring sites as well as the
72 limited spatial representativeness (Liu et al., 2017b; Liu et al., 2017a). Satellite NH_3
73 retrievals are an important complement to gain the global distribution of NH_3
74 concentrations with a high spatial resolution (Van Damme et al., 2014c). NH_3 can be
75 measured by several satellite instruments including the Infrared Atmospheric
76 Sounding Interferometer (IASI), Atmospheric Infrared Sounder (AIRS), Cross-track
77 Infrared Sounder (CrIS) and Tropospheric Emission Spectrometer (TES). TES using
78 the thermal infrared spectral range has sparser spatial coverage compared to IASI,
79 CrIS and AIRS (Shephard et al., 2011; Zhang et al., 2017a). A recent study (Kharol et
80 al., 2018) reported the dry NH_3 depositions in North America, and found -15%
81 underestimation in CrIS surface NH_3 concentrations (using three fixed NH_3 profiles
82 considering unpolluted, moderate and polluted conditions) compared with the
83 measurements from the AMoN-US during the warm months (from April to
84 September). Warner et al. reported the global AIRS NH_3 concentrations at 918hPa
85 (approximately 700-800 m) at 1° latitude \times 1° longitude grids, and found NH_3
86 concentrations increased in the major agricultural regions during 2003-2015 (Warner
87 et al., 2017). The IASI NH_3 measurements have been validated with NH_3 columns
88 measured by the Fourier transform infrared spectroscopy (FTIR), ground-based NH_3



89 measurements, NH₃ emissions and atmospheric chemistry transport models (CTMs)
90 (Dammers et al., 2016; Van Damme et al., 2014c; Van Damme et al., 2014a; Whitburn
91 et al., 2016).
92 Apart from satellite retrievals, CTMs are also powerful tools to investigate
93 spatiotemporal variability of surface NH₃ concentrations in the atmosphere. Schiferl et
94 al. evaluated the modelled NH₃ concentrations during 2008-2012 from GEOS-Chem,
95 and found an approximately 26% underestimation compared with the ground-based
96 measurements, which can be related to the relatively large uncertainties in NH₃
97 emissions used for driving GEOS-Chem (Schiferl et al., 2015). Zhu et al. used the
98 GEOS-Chem constrained by TES measurements to estimate surface NH₃
99 concentration during 2006-2009, and found an improvement in comparison with the
100 ground-based measurements in the United States (Zhu et al., 2013). Schiferl et al.
101 used the airborne observations to validate the simulated NH₃ concentrations in 2010
102 from GEOS-Chem, and revealed reasonably simulated NH₃ vertical profiles compared
103 with the aircraft measurements but with an underestimation in surface NH₃
104 concentrations in California (Schiferl et al., 2014). A number of previous studies have
105 used satellite NO₂ columns to estimate the surface NO₂ concentrations combining
106 NO₂ vertical profiles from CTMs (Geddes et al., 2016; Lamsal et al., 2013; Nowlan et
107 al., 2014; Liu et al., 2017c). The methods of using the vertical profiles to convert
108 satellite-retrieved columns to surface concentrations have been proven successful for
109 SO₂ and NO₂ (Geddes et al., 2016; Geng et al., 2015; Lamsal et al., 2008; Nowlan et al.,
110 2014). CTMs can provide valuable information of NH₃ vertical profiles (Whitburn et
111 al., 2016; Liu et al., 2017b), and IASI-derived surface NH₃ concentrations combining
112 NH₃ vertical profiles from CTMs in China and Europe were evaluated previously (Liu
113 et al., 2017b; Graaf et al., 2018). This study followed these studies to estimate the
114 satellite-derived global surface NH₃ concentrations using IASI NH₃ retrievals and the
115 vertical profiles from GEOS-Chem, and the present study aims to estimate the global
116 surface NH₃ concentration from a satellite perspective.

117



118 **Data and Methods**

119 **IASI NH₃ measurements**

120 The Infrared Atmospheric Sounding Interferometer (IASI) is a passive instrument
121 measuring infrared radiation within the spectral range of 645-2769 cm⁻¹. The IASI-A
122 instrument is on board of the MetOp-A satellite launched in 2006 covering the globe
123 twice a day with an elliptical spatial resolution of approximately 12 by 12 kilometers,
124 and cross the equator at 09:30 and 21:30 local times (Van Damme et al., 2014b). We
125 used the daytime IASI NH₃ measurements due to the larger positive thermal contrast
126 detected by satellite instruments leading to smaller errors compared to the nighttime
127 data (Van Damme et al., 2014b). In this work, we used the IASI NH₃ columns
128 products (ANNI-NH3-v2.2R-I) during 2008-2016 (Van Damme et al., 2017) to
129 estimate the global surface NH₃ concentrations. The ANNI-NH3-v2.2R-I datasets
130 were developed by converting spectral HRI (hyperspectral range index) to NH₃
131 columns through an Artificial Neural Network for IASI (ANNI) algorithm (Whitburn
132 et al., 2016). This algorithm considered the influence of the NH₃ vertical profiles,
133 pressure, humidity and temperature profiles. The NH₃ vertical profile information
134 used to generate the ANNI NH₃ columns were retrieved from GEOS-Chem, which
135 integrates H₂SO₄-HNO₃-NH₃ aerosol thermodynamics mechanism (Whitburn et al.,
136 2016; Van Damme et al., 2017). The IASI NH₃ columns used in this study were
137 processed into the monthly data at 0.25° latitude × 0.25° longitude grids by the
138 arithmetic averaging method (Van Damme et al., 2017; Whitburn et al., 2016; Liu et al.,
139 2017a).

140

141 **Surface NH₃ measurements**

142 To evaluate our satellite-derived global surface NH₃ concentrations, we collected
143 available surface NH₃ measurements on a regional scale in 2014. In China, we used
144 the national measurements from the Chinese Nationwide Nitrogen Deposition
145 Monitoring Network (NNDMN). Surface NH₃ concentrations in the NNDMN were
146 measured by both ALPHA (Adapted Low-cost, Passive High Absorption) and DELTA



147 (Denuder for Long-Term Atmospheric sampling) systems. The detailed descriptions
148 on the NNDMN have been described in a previous study (Xu et al., 2015). In the US,
149 we used the measurements from the AMoN-US, downloaded from the website:
150 <http://nadp.sws.uiuc.edu/AMoN/>. Surface NH₃ concentrations in the AMoN-US were
151 measured by the radiello diffusive sampler (<http://www.radiello.com>) as a simple
152 diffusion-type sampler collected every 2 weeks (Li et al., 2016). We calculated annual
153 surface NH₃ concentrations by averaging all the measurements (every 2 weeks), and
154 then used them to compare with satellite-derived surface NH₃ concentrations. In
155 Europe, we used the measurements from the EMEP network
156 (<https://www.nilu.no/projects/ccc/emepdata.html>). The EMEP is composed of
157 multiple national networks in Europe, thus the measured systems differs among
158 different national networks.

159

160 **GEOS-Chem model**

161 We used GEOS-Chem version 11-01 as the chemical transport model to calculate
162 global NH₃ vertical profiles (using the year of 2014 as a case study in the results and
163 discussion). It has a spatial resolution of 2° latitude × 2.5° longitude × 47 vertical
164 layers spanning over Earth's surface and about 80 km above it. It is driven by the
165 meteorological field data of the GEOS-FP (forward-processing) products, which were
166 produced by NASA GMAO (Global Modelling and Assimilation Office)
167 (<https://gmao.gsfc.nasa.gov/>). Here we modelled the NH₃ vertical profiles using
168 GEOS-Chem, and used the monthly averages for analysis. The global NH₃ emissions
169 in GEOS-Chem are based on the EDGAR (Emissions Database for Global
170 Atmospheric Research) v4.2 (<http://edgar.jrc.ec.europa.eu/overview.php?v=42>), while
171 the regional emissions are replaced with MIX inventory for East Asia (Li et al., 2017a)
172 (<http://www.meicmodel.org/dataset-mix.html>), EMEP inventory for Europe
173 (<http://www.emep.int/>), NEI (National Emissions Inventory, 2011) for the US
174 (<https://www.epa.gov/air-emissions-inventories>) and CAC (Criteria Air Contaminant)
175 inventory for Canada (<http://www.acrd.bc.ca/criteria-air-contaminants>). The biomass



176 burning emissions are from Fire INventory from NCAR version 1.0 (FINNv1)
177 including agricultural fires, wildfire and pre-scribed burning (Wiedinmyer et al.,
178 2011). The GEOS-Chem simulates a comprehensive atmospheric
179 NO_x-O₃-VOC-aerosol system (Mao et al., 2013). The thermodynamic equilibrium of
180 NH₃-H₂SO₄-HNO₃ system is simulated by the ISORROPIA II model (Fountoukis and
181 Nenes, 2007;Pye et al., 2009). The modelling of wet deposition is described by a
182 previous study (Liu et al., 2001) with updates from the studies (Amos et al.,
183 2012;Wang et al., 2011). Dry deposition of particles follows the size-segregated
184 treatment (Zhang et al., 2001) and gaseous dry deposition follows the framework
185 (Wesely, 1989) with updates from a previous study (Wang et al., 1998). We archive
186 the output daily averages of NH₃ concentrations as well as the averages between 9 and
187 10 am, which corresponds to the local crossing time of IASI (9:30 am). The
188 relationship between NH₃ concentration at 9-10 am and the daily averages derived
189 from the GEOS-Chem was used to convert the satellite observed NH₃ column to daily
190 averages (Nowlan et al., 2014).

191

192 **Estimation of surface NH₃ concentrations**

193 We estimated global surface NH₃ concentrations using the IASI NH₃ columns as well
194 as the GEOS-Chem. We took into account the advantages of IASI NH₃ columns with
195 high spatial resolutions and the GEOS-Chem with vertical profiles. The GEOS-Chem
196 outputs include 47 layers, which are not continuous in the vertical direction. To gain
197 the continuous vertical NH₃ profile, we used the Gaussian function to fit the 47 layers'
198 NH₃ concentrations. The height of each grid box used here was calculated at the
199 middle height of each layer rather than the top height of each layer. A three-parameter
200 Gaussian function was used to fit NH₃ vertical profiles at each grid box from the
201 GEOS-Chem in the previous studies (Whitburn et al., 2016;Liu et al., 2017b) :

$$202 \quad \rho = \rho_{max} e^{-\left(\frac{Z-Z_0}{\sigma}\right)^2} \quad (1)$$

203 where ρ is NH₃ concentrations at the layer height Z ; ρ_{max} is the maximum NH₃
204 concentrations at the height z_0 ; σ is an indicator for the spread or thickness of the



205 NH₃ concentrations.

206 This study expanded the equation (1) to fit NH₃ vertical profiles at each grid box by
207 the following equation (Liu et al., 2017b):

$$208 \quad \rho = \sum_{i=1}^n \rho_{max,i} e^{-\left(\frac{z-z_{0,i}}{\sigma_i}\right)^2} \quad (2)$$

209 where n ranges from 1 to 6. If n equals 1, the equation (2) is the same as the equation
210 (1); if n is greater than 1, the equation (2) is the multiple three-parameters Gaussian
211 items. We determined the value of n that can simulate the NH₃ vertical profiles with
212 best performance at each grid box using the determining coefficients of R-Square (R²).

213 Once the NH₃ vertical profiles were determined at each grid box, we can extrapolate
214 NH₃ concentrations at any height from the GEOS-Chem ($G_{GEOS-Chem}$).

215 We then aggregated the IASI NH₃ columns Ω_{IASI} (0.25° latitude × 0.25° longitude)
216 to the GEOS-Chem grid size $\overline{\Omega_{IASI}}$ (2° latitude × 2.5° longitude) by the averaging
217 method. We have the following equation (Lamsal et al., 2008):

$$218 \quad \overline{G_{IASI9-10}} = \frac{G_{GEOS-Chem}}{\Omega_{GEOS-Chem}} \times \overline{\Omega_{IASI9-10}} \quad (3)$$

219 where $\overline{G_{IASI9-10}}$ is the satellite-derived surface NH₃ concentrations at a GEOS-Chem
220 grid size at 9-10am; $\frac{G_{GEOS-Chem}}{\Omega_{GEOS-Chem}}$ is the ratio of surface NH₃ concentrations to NH₃
221 columns calculated from GEOS-Chem; $\overline{\Omega_{IASI9-10}}$ is the average IASI NH₃ columns
222 at a GEOS-Chem grid at 9-10am.

223 We found a high correlation (R=0.96 and p=0.000) between the surface NH₃
224 concentrations and NH₃ columns based on the GEOS-Chem outputs (**Fig. S1**). Then
225 we used the satellite-derived scaling factor to downscale the satellite-derived surface
226 NH₃ concentrations at a GEOS-Chem grid by using the following ratio:

$$227 \quad R_{IASI} = \frac{\Omega_{IASI}}{\overline{\Omega_{IASI}}} \quad (4)$$

$$228 \quad G_{IASI9-10} = \overline{G_{IASI9-10}} \times R_{IASI} \quad (5)$$

229 where R_{IASI} is the scaling factor. $G_{IASI9-10}$ is the satellite-derived surface NH₃
230 concentrations at a satellite IASI grid size (0.25° latitude × 0.25° longitude) at 9-10am.

231 To convert the instantaneous satellite-derived surface NH₃ concentrations G_{IASI} to



232 daily average surface NH_3 concentrations, we followed the methods (Nowlan et al.,
233 2014):

$$234 \quad G_{IASI}^* = \frac{G_{GEOS-Chem}^{1-24}}{G_{GEOS-Chem}^{9-10}} \times G_{IASI_{9-10}} \quad (6)$$

235 where G_{IASI}^* is the daily average surface NH_3 concentrations, and $\frac{G_{GEOS-Chem}^{1-24}}{G_{GEOS-Chem}^{9-10}}$ is the
236 ratio of the GEOS-Chem surface NH_3 concentrations at the daily average to the
237 average of 9-10 am.

238

239 Results and Discussion

240 NH_3 vertical profiles from GEOS-Chem

241 NH_3 emitted from the surface can be transported horizontally or vertically, and its
242 concentrations may show a certain gradient in the vertical and horizontal directions (E.
243 et al., 1997;Rozanov et al., 2005). There are generally two types of shapes of NH_3
244 vertical profiles (**Fig. S2**) from aircraft measurements (Li et al., 2017b;Tevlin et al.,
245 2017) and CTMs (Whitburn et al., 2016;Liu et al., 2017b). One is representative for
246 the vertical profile with maximum NH_3 concentrations at a certain height ($z_0>0$) and
247 the other is representative for the vertical profile with maximum NH_3 concentrations
248 near the earth surface ($z_0=0$). In this study, the vertical profiles of NH_3 were fitted
249 based on the 47 layers' outputs by GEOS-Chem in 2014 at a monthly scale. **Fig. S3**
250 shows the spatial distribution of NH_3 concentrations in the first and fifth layers
251 simulated by GEOS-Chem in January 2014. NH_3 concentrations in the fifth layer are
252 significantly lower than those in the first layer, suggesting that NH_3 concentrations
253 decrease with increasing layers (or altitude), especially in NH_3 hotspot regions (such
254 as eastern China, India, western Europe and eastern US). The average difference of
255 NH_3 concentrations between the first and fifth layers on the land is $0.34 \mu\text{g N m}^{-3}$. The
256 average NH_3 concentrations in the first and fifth layers in eastern China, India,
257 western Europe and eastern US were 2.76, 7.28, 0.55 and $0.31 \mu\text{g N m}^{-3}$, respectively.

258

259 To more vividly depict the vertical profiles of NH_3 , we show NH_3 vertical
260 concentrations with cross-section drawn at 37°N in January, 2014 (**Fig. S4**). High NH_3



261 concentrations are mainly concentrated in the 1-10 layers, and show a significant
262 decrease trend with the increasing altitude, which is consistent with the aircraft
263 measurements (E. et al., 1997; Lin et al., 2014; Levine et al., 1980; Shephard and
264 Cady-Pereira, 2015; Li et al., 2017b; Tevlin et al., 2017). NH_3 vertical profiles were
265 fitted by Gaussian function (2-6 terms) based on the 47 layers' NH_3 concentrations
266 from the GEOS-Chem, and the fitting accuracy was determined by R^2 . We found that
267 the NH_3 vertical profiles on the land between 60°N and 55°S can be well modelled
268 using Gaussian function (R^2 higher than 0.90) (**Fig. 1**). Previous studies also found
269 high accuracy using the Gaussian function to simulate the NH_3 vertical profiles in
270 China and globally (Whitburn et al., 2016; Liu et al., 2017b).

271

272 **Validation of satellite-derived surface NH_3 concentrations**

273 NH_3 vertical profiles were used to convert IASI NH_3 columns to surface NH_3
274 concentrations. **Fig. 2** shows the IASI-derived global surface NH_3 concentrations on
275 the land at 0.25° latitude \times 0.25° longitude grids in 2014. IASI-derived surface NH_3
276 concentrations capture the general spatial pattern of surface NH_3 concentrations fairly
277 well in 2014 in regions with relatively intensive monitoring sites ($R^2=0.76$ and
278 $\text{RMSE}=1.50 \mu\text{g N m}^{-3}$ in **Fig. 2 and Fig. 3**). The overall mean of satellite-derived
279 surface NH_3 concentrations in 2014 at the measured sites was $2.52 \mu\text{g N m}^{-3}$ and was
280 close to the average of measured surface NH_3 concentrations ($2.51 \mu\text{g N m}^{-3}$) in 2014.
281 IASI-derived surface NH_3 concentrations gained higher consistency with the
282 ground-based measurements in China ($R^2=0.71$ and $\text{RMSE}=2.6 \mu\text{g N m}^{-3}$) than the US
283 ($R^2=0.45$ and $\text{RMSE}=0.76 \mu\text{g N m}^{-3}$) and Europe ($R^2=0.45$ and $\text{RMSE}=0.86 \mu\text{g N m}^{-3}$)
284 at a yearly scale. This might be due to the fact that for high concentrations in a region
285 (associated with high thermal contrast) can be more reliably detected by IASI (Van
286 Damme et al., 2014a). Similarly, we also compared the surface NH_3 concentrations (at
287 the first layer) simulated by GEOS-Chem with the monitoring results ($R^2=0.54$ and
288 $\text{RMSE}=2.14 \mu\text{g N m}^{-3}$ in **Fig. 3**). In general, IASI-derived surface NH_3 concentrations
289 had better consistency with the ground-based measurements than those from



290 GEOS-Chem over China, the US and Europe. The relatively low accuracy from
291 GEOS-Chem was likely due to the coarse model resolutions as well as the poor
292 spatiotemporal representations of NH_3 emissions, as suggested by a previous study
293 (Zhang et al., 2018).

294

295 A known limitation of IASI NH_3 retrievals is lack of the vertical profile information.
296 A previous study (Van Damme et al., 2014a) used the fixed profiles on the land to
297 convert the IASI NH_3 columns to surface NH_3 concentrations. Using the fixed profiles
298 can cause large uncertainties for estimating surface NH_3 concentrations. In this work,
299 we utilized the advantages of CTMs and considered the spatial variability of the
300 vertical profiles, and proves that IASI NH_3 columns are powerful to predict the
301 surface NH_3 concentrations combining the vertical profiles simulated by Gaussian
302 function.

303

304 Through the Gaussian simulation of NH_3 vertical profiles, we are able to evaluate the
305 sensitive regions of surface NH_3 concentrations with respect to different heights. **Fig.**
306 **S5** shows the spatial distribution of the difference of NH_3 concentrations between
307 40m and 60m (about the middle height of the first layer in GEOS-Chem). In general,
308 in strong NH_3 emission regions, there is a relatively large difference in surface NH_3
309 concentrations such as, for instance, in eastern China and northwestern India (can be
310 up to $3 \mu\text{g N m}^{-3}$); subsequently, a middle difference ($2\text{-}3 \mu\text{g N m}^{-3}$) occurs in eastern
311 and middle China, northern India and northern Italy. Except above mentioned regions,
312 the difference of NH_3 concentrations between 40m and 60m is generally lower $0.5 \mu\text{g}$
313 N m^{-3} .

314

315 **Spatial distributions of satellite-derived surface NH_3 concentrations**

316 **Fig. 4** shows the spatial distributions of surface NH_3 concentrations in China, US and
317 Europe in 2014. The overall mean surface NH_3 concentrations over China were 2.38
318 $\mu\text{g N m}^{-3}$, with the range of $0.22\text{-}13.11 \mu\text{g N m}^{-3}$. We found large areas in eastern



319 China, Sichuan Basin and northwestern Xinjiang with surface NH_3 concentrations
320 greater than $8 \mu\text{g N m}^{-3} \text{ y}^{-1}$, which were in agreement with the spatial distributions of
321 the croplands in China (**Fig. S6**). It is not surprising that high surface NH_3
322 concentrations occurred in eastern China and Sichuan Basin because the major
323 Chinese croplands are distributed there, as the major source of NH_3 emissions with
324 frequent N fertilizer applications. Overall, there was a significant linear correlation
325 between surface NH_3 concentration and N fertilization in China ($R^2=0.65$, $p=0.000$ in
326 **Fig. 5**). The hotspots also occurred in northwestern Xinjiang surrounding the cropland
327 areas, which may be related to the dry climate that can maintain NH_3 in the gaseous
328 state for a longer time, providing climate conditions for the long distance transmission
329 of NH_3 . Recent national measurement work (Pan et al., 2018) also revealed high
330 surface NH_3 concentrations in northwestern Xinjiang, confirming the rationality of the
331 IASI-derived estimates.

332

333 In the US, the overall mean surface NH_3 concentrations were $1.52 \mu\text{g N m}^{-3} \text{ y}^{-1}$, with
334 the range of $0.14\text{-}10.60 \mu\text{g N m}^{-3}$. The surface NH_3 hotspots were generally
335 distributed in the croplands in the central and eastern US (such as Ohio, Illinois, South
336 Dakota, Nebraska, Kansas, Minnesota and North Dakota), as well as in some small
337 areas in western coastal regions (such as California and Washington). In particular, the
338 San Joaquin Valley (SJV) in California (an agricultural land) had the highest surface
339 NH_3 concentrations greater than $4 \mu\text{g N m}^{-3}$. The NH_3 source in SJV was from
340 livestock and mineral N fertilizer, which accounted for 74% and 16% of total NH_3
341 emissions, respectively (Simon et al., 2008). Except the SJV in California, the annual
342 surface NH_3 concentrations in the croplands were mostly within the range of $1\text{-}3 \mu\text{g N}$
343 m^{-3} , which were much lower than those in eastern China (mostly within the range of
344 $4\text{-}10 \mu\text{g N m}^{-3}$). Compared with the spatial distribution of N fertilization, the hotspots
345 of surface NH_3 concentration can basically reflect the distribution of high N
346 fertilization ($R^2=0.30$, $p=0.000$ in **Fig 4 and Fig. 5**).

347

348 In Europe, the overall mean surface NH_3 concentrations were $1.8 \mu\text{g N m}^{-3}$, with the



349 range of 0.04-9.49 $\mu\text{g N m}^{-3}$. High surface NH_3 concentrations were distributed
350 widespread in the croplands, especially in the western regions with values greater than
351 4 $\mu\text{g N m}^{-3}$, such as Northern Italy (Milan and its surrounding areas), Switzerland,
352 central and southern Germany, Eastern France (Paris and its surrounding areas) and
353 Poland. Overall, there was also a significant linear correlation between surface NH_3
354 concentration and N fertilization ($R^2=0.17$, $p=0.000$) in Europe, reflecting the
355 importance of N fertilization on surface NH_3 concentration.

356

357 NH_3 is the most abundant alkaline gas in the atmosphere, and has implications to
358 neutralize acidic species (such as H_2SO_4 and HNO_3) to form ammonium salts (such as
359 $(\text{NH}_4)_2\text{SO}_4$ and NH_4NO_3). Ammonium salts are the important inorganic N
360 components in $\text{PM}_{2.5}$, which can reduce regional visibility and contribute to human
361 disease burden (Van et al., 2015; Yu et al., 2007). Comparing surface NH_3
362 concentrations with $\text{PM}_{2.5}$ can benefit the understanding of the sources and the
363 mixture of air pollution. The spatial distribution of satellite-derived $\text{PM}_{2.5}$ (dust and
364 sea-salt removed) in 2014 (**Fig. S7**) gained from a previous study (Van et al., 2016)
365 was compared with the satellite-derived surface NH_3 concentrations in 2014. On the
366 other hand, NO_2 is also an important precursor of nitrate salts in $\text{PM}_{2.5}$. We also
367 included the satellite-derived surface NO_2 concentrations (**Fig. S7**) from a previous
368 study (Geddes et al., 2016) to compare with surface NH_3 and $\text{PM}_{2.5}$ concentrations.

369

370 The hotspots of surface NH_3 concentrations were highly linked with the hotspots of
371 $\text{PM}_{2.5}$. The most severe pollution occurred in the eastern China with annual average
372 $\text{PM}_{2.5}$ exceeding 50 $\mu\text{g m}^{-3}$ (much higher than 35 $\mu\text{g m}^{-3}$ as the level 2 annual $\text{PM}_{2.5}$
373 standard set by World Health Organization Air Quality Interim Target-1), and annual
374 average surface NH_3 and NO_2 concentrations greater than 8 $\mu\text{g N m}^{-3}$ and 4 $\mu\text{g N m}^{-3}$,
375 respectively. A previous study (Xu et al., 2017) reported that the secondary inorganic
376 aerosols of NH_4^+ and NO_3^- can account for 65% of $\text{PM}_{2.5}$ based on the measurements
377 in three sites in Beijing. NH_3 and NO_2 are the most important precursors of nitrate
378 salts and ammonium salts, and certainly contribute to the severe pollution in the



379 eastern China. The second severe pollution occurred in the northern India with annual
380 average $\text{PM}_{2.5}$ and surface NH_3 concentrations exceeding $40 \mu\text{g m}^{-3}$ and $4 \mu\text{g N m}^{-3}$
381 respectively (surface NO_2 concentrations less than $1 \mu\text{g N m}^{-3}$). The major source of
382 NH_3 in northern India was from agricultural activities and livestock waste
383 management (Warner et al., 2016). The hotspots of surface NH_3 concentrations in the
384 central and eastern US were highly related to the hotspots of $\text{PM}_{2.5}$. The annual
385 average $\text{PM}_{2.5}$ is less than $10 \mu\text{g m}^{-3}$ (the first level set by World Health Organization)
386 in the most areas of the US, and only small areas had $\text{PM}_{2.5}$ greater than $10 \mu\text{g m}^{-3}$.
387 Similarly, in western Europe, the hotspots of high surface NH_3 and NO_2
388 concentrations (greater than $3 \mu\text{g N m}^{-3}$) were consistent with the hotspots of $\text{PM}_{2.5}$
389 (greater than $20 \mu\text{g m}^{-3}$).

390

391 **Seasonal variations of satellite-derived surface NH_3 concentrations**

392 To investigate the seasonal variations of surface NH_3 concentrations, we took the
393 monthly surface NH_3 concentrations in 2014 as a case study (**Fig. 6**), and analyzed the
394 seasonal surface NH_3 concentrations in hotspot regions including East China (ECH),
395 Sichuan and Chongqing (SCH), Guangdong (GD), Northeast India (NEI), East US
396 (EUS) and West Europe (WEU) (**Fig. 7**).

397

398 Seasonal mean IASI-derived surface NH_3 concentrations vary by more than 2 orders
399 of magnitude in hotspot regions, such as the eastern China and eastern US. In China,
400 high surface NH_3 concentrations occurred in spring (March, April and May) and
401 summer (June, July and August) in East China (ECH), Sichuan and Chongqing (SCH),
402 Guangdong (GD). This may be due to two major reasons. First, the timing of the
403 mineral N fertilizer or manure application occurred in summer or spring in the
404 croplands (Paulot et al., 2014). A previous study (Huang et al., 2012) also suggested a
405 summer peak in NH_3 emissions in China, which was consistent with the summer peak
406 in surface NH_3 concentrations. Second, the temperature in warm months is highest in
407 one year, which favors the volatilization of ammonium ($\text{NH}_4^+ + \text{OH}^- \rightarrow \text{NH}_3 + \text{H}_2\text{O}$). In



408 the eastern US (EUS), high surface NH_3 concentrations appeared in warm months
409 (from March to August, **Fig. 7**) with the maximum in May due to higher temperature
410 and emissions in vast croplands, where the agricultural mineral N fertilizers dominate
411 the NH_3 emissions. A previous study also implied a spring peak in NH_3 emissions in
412 the eastern US (Gilliland et al., 2006). Since the spatial patterns of high surface NH_3
413 concentrations are highly linked with the spatial distributions of croplands, seasonal
414 surface NH_3 concentrations mainly reflects the timing of N fertilizers in the croplands.
415 In western Europe, surface NH_3 concentrations is low in January and February, rising
416 in March and reaching its maximum, keeping high from March to June, then declining
417 from June to December (**Fig. 7**). High NH_3 concentrations appeared from March to
418 June, mainly affected by higher temperature and frequent N fertilization (Van Damme
419 et al., 2014b; Paulot et al., 2014; Van Damme et al., 2015; Whitburn et al., 2015).

420

421 To identify the major regions of biomass burning that may affect the spatial
422 distribution of surface NH_3 concentrations, we used the fire products from the
423 moderate resolution imaging spectroradiometer (MODIS) on board the NASA Aqua
424 and Terra. The MODIS climate modeling grid (CMG) global monthly fire location
425 product (level 2, collection 6) developed by the University of Maryland included
426 geographic location of fire, raw count of fire pixels and mean fire radiative power
427 (Giglio et al., 2015). We used the Aqua and Terra CMG fire products on a monthly
428 scale at a spatial resolution of 0.5° latitude \times 0.5° longitude in 2014, and the fire pixel
429 counts were used to identify the hotspot regions of biomass burning. In the major
430 hotspots with frequent fires (mostly in the southern hemisphere), the biomass burning
431 controlled the seasonal surface NH_3 concentrations (**Fig. S8 and Fig. S9**), such as, for
432 instance, Africa north of equator, Africa south of equator and central South America.
433 Apart from the large areas with frequent fires in the southern hemisphere, we also
434 demonstrated the relationship of biomass burning and surface NH_3 concentrations in
435 China, US and Europe, and selected six typical regions in China (CH1 and CH2), US
436 (US1 and US2) and Europe (EU1 and EU2) (**Fig. 8**) to analyze the monthly variations
437 of fire counts and surface NH_3 concentrations.



438

439 In China, the first region (CH1) covers the major cropland areas in northern China
440 including Shandong, Henan and northern Jiangsu Provinces. The fires counts
441 were mainly from the crop straw burning, which contributes large to surface NH_3
442 concentrations. Both surface NH_3 concentrations and fire counts were found in June
443 likely related to the crop straw burning in this agricultural regions. Notably, despite a
444 decline in fire counts in July, the surface NH_3 concentrations in July did not decrease,
445 probably due to mineral N fertilization for new planted crops (CH1 is typical for
446 spring and summer corn rotations) as well as the high temperature favoring NH_3
447 volatilization in July. The second region (CH2) is typical for the rice cultivation area
448 in the southern China, where the rice was normally planted in June or July with
449 frequent mineral N fertilization. Thus, the highest surface NH_3 concentrations
450 occurred in June and July. This region is also typical for the winter wheat and summer
451 rice rotations, and the wheat is normally harvested from May to July, which can lead
452 to frequent fire counts there. Despite the more frequent fires in the second region than
453 the first region, the surface NH_3 concentrations in CH2 were much lower than those in
454 CH1. This may be due to the wetter climate and more frequent precipitation events in
455 CH2 than in CH1, resulting in higher scavenging of surface NH_3 concentrations into
456 water.

457

458 US1 is a region typical for forest land in the US, and the fire counts are certainly from
459 the forest fires or anthropogenic biomass burning. The monthly variations of surface
460 NH_3 concentrations were consistent with the monthly variations of MODIS fire counts,
461 which peaked in August with high temperature. Instead, US2 is a region typical for
462 mixed agricultural and forest lands, which can be influenced by both potential mineral
463 N fertilization and anthropogenic biomass burning or forest fires. It is clear to see that
464 there is a peak in surface NH_3 concentrations in October resulting from the biomass
465 burning because of the same peak in fire counts in October. However, there is also an
466 apparent peak in surface NH_3 concentrations in May, which may result from the
467 mineral N fertilization in this region. In Europe, the selected two regions of EU1 and



468 EU2 are mainly covered by crops, vegetables as well as forests. For EU2, the monthly
469 variations of surface NH_3 concentrations were consistent with the monthly variations
470 of MODIS fire counts, which peaked in August with high temperature, implying that
471 the biomass burning may control the seasonal surface NH_3 concentrations. For EU1,
472 there were two peaks of surface NH_3 concentrations including April and August. The
473 August peak can be related to the biomass burning because of the high fire counts,
474 while the April peak may be related to the agricultural fertilizations for the spring
475 crops.

476

477 **Trends in surface NH_3 concentrations in China, the US and Europe**

478 Time series of nine years' (2008-2016) IASI-derived surface NH_3 concentrations have
479 been fitted using the linear regression method (Geddes et al., 2016; Richter et al., 2005)
480 for all grids on the land. The annual trend (the slope of the linear regression model) is
481 shown in **Fig. 9**. A significant increase rate of surface NH_3 concentrations ($>0.2 \mu\text{g N}$
482 $\text{m}^{-3} \text{y}^{-1}$) appeared in eastern China, and a middle positive trend ($0.1\text{-}0.2 \mu\text{g N m}^{-3} \text{y}^{-1}$)
483 occurred in northern Xinjiang, corresponding to its frequent agricultural activities for
484 fertilized crops and dry climate (Warner et al., 2017; Liu et al., 2017b; Xu et al.,
485 2015; Huang et al., 2012). The large increase in eastern China was consistent with the
486 results revealed by AIRS NH_3 data (Warner et al., 2017). China's NH_3 emissions
487 increased significantly from 2008 to 2015, with an increase rate of $1.9\% \text{y}^{-1}$, which
488 was mainly driven by eastern China (Zhang et al., 2017b). In addition, the increase in
489 surface NH_3 concentrations in eastern China may be also linked with the decreased
490 NH_3 removal due to the decline in acidic gases (NO_2 and SO_2) (Liu et al., 2017a; Xia
491 et al., 2016). NH_3 can react with nitric acid and sulfuric acid to form ammonia sulfate
492 and ammonia nitrate aerosols. The reduction of acidic gases leads to the reduction of
493 NH_3 conversion to ammonia salts in the atmosphere, which may lead to the increase
494 of NH_3 in the atmosphere (Liu et al., 2017a; Li et al., 2017b). China's SO_2 emissions
495 decreased by about 60% in 2008-2016, which led to a 50% decrease in surface
496 SO_2 concentrations simulated by WRF model, and then resulted in a 30% increase in



497 surface NH₃ concentrations (Liu et al., 2018).

498

499 In the US, the NH₃ increase was found in agricultural regions in middle and eastern
500 regions with an annual increase rate of lower than 0.10 μg N m⁻³ y⁻¹, which was
501 consistent with the results of AIRS NH₃ data for a longer time period (2003-2016)
502 (Warner et al., 2017), while we concerned the timespan of 2008-2016 from IASI
503 retrievals. Based on the simulation data of CMAQ model, it is also found that NH₃
504 increased significantly in the eastern US from 1990 to 2010, which is inconsistent
505 with the significant downward trend of NO_x emissions (Zhang et al., 2018). This NH₃
506 increase in eastern US is likely due to the lack of NH₃ emission control policy as well
507 as the decreased NH₃ removal due to the decline in acidic gases (NO₂ and SO₂)
508 (Warner et al., 2017; Li et al., 2016). As NH₃ is an uncontrolled gas in the US, NH₃
509 emissions have continuously increased since 1990, and by 2003 NH₃ emissions had
510 begun to dominate the inorganic N emissions (NO_x plus NH₃) (Zhang et al., 2018).
511 For the western Europe, the trend was close to 0 in most regions although we can
512 observe the NH₃ increase in many points with small positive trend of lower than 0.1
513 μg N m⁻³ y⁻¹. Compared with the trend of surface NH₃ concentrations in China and the
514 US, the change of surface NH₃ concentrations in western Europe is more stable,
515 which may be related to the mature NH₃ reduction policies and measures in Europe.
516 Since 1990, Europe has implemented a series of agricultural NH₃ emission reduction
517 measures, and NH₃ emissions decreased by about 29% between 1990 and 2009
518 (Tørseth et al., 2012). For example, due to serious N eutrophication, the Netherlands
519 has taken measures to reduce NH₃ emissions by nearly two times in the past 20 years,
520 while maintaining a high level of food production (Dentener et al., 2006). The N
521 fertilizer use in Europe has decreased widespread according to the data from the
522 World Bank (<http://data.worldbank.org/indicator/AG.CON.FERT.ZS>) with an annual
523 decrease of -8.84~-17.7 kg ha⁻¹ y⁻¹ in fertilizer use in Europe (Warner et al., 2017).

524



525 **Conclusions**

526 The IASI-derived global surface NH₃ concentrations during 2008-2016 were inferred
527 based on IASI NH₃ column measurements as well as NH₃ vertical profiles from the
528 GEOS-Chem in this study. Global NH₃ vertical profiles on the land from the
529 GEOS-Chem can be well modelled by the Gaussian function between 60°N and 55°
530 S with R² higher than 0.90. The IASI-derived surface NH₃ concentrations were
531 compared to the in situ measurements over China, the US and Europe. One of the
532 major findings is that a relatively high predictive power for annual surface NH₃
533 concentrations was achieved through converting IASI NH₃ columns using modelled
534 NH₃ vertical profiles, and the validation with the ground-based measurements shows
535 that IASI-derived surface NH₃ concentrations had higher accuracy in China than the
536 US and Europe. High surface NH₃ concentrations were found in the croplands in
537 China, US and Europe, and surface NH₃ concentrations in the croplands in China
538 were approximately double than those in the US and Europe. Seasonal mean
539 IASI-derived surface NH₃ concentrations vary by more than 2 orders of magnitude in
540 hotspot regions, such as the eastern China and eastern US. The linear trend analysis
541 shows that a significant positive increase rate of above 0.2 μg N m⁻³ y⁻¹ appeared in
542 the eastern China during 2008-2016, and a middle increase trend (0.1-0.2 μg N m⁻³ y⁻¹)
543 occurred in northern Xinjiang Province. In the US, the NH₃ increase was found in
544 agricultural regions in middle and eastern regions with an annual increase rate of
545 lower than 0.10 μg N m⁻³ y⁻¹.

546

547 **Author contributions**

548 LL and XZ designed the research; WX and XL's group conducted the field work in
549 China; LL prepared IASI NH₃ products; LL and AW conducted model simulations;
550 LL, WX, LZ, XW and ZW performed the data analysis and prepared the figures; LL,
551 AW and XZ wrote the paper, and all coauthors contribute to the revision.

552



553 **Acknowledgements**

554 We acknowledge the free use of IASI NH₃ data from the Atmospheric Spectroscopy
555 Group at Université libre de Bruxelles (ULB). We thank Dr. Jeffrey A. Geddes for the
556 help of using the GEOS-Chem in this work. This study is supported by the National
557 Natural Science Foundation of China (No. 41471343, 41425007 and 41101315) and
558 Doctoral Research Innovation Fund (2016CL07) as well as the Chinese National
559 Programs on Heavy Air Pollution Mechanisms and Enhanced Prevention Measures
560 (Project No. 8 in the 2nd Special Program).

561

562 **Data availability**

563 The IASI NH₃ satellite datasets are available at: <http://iasi.aeris-data.fr/NH3>. The
564 ground-based NH₃ measurements in Chinese Nationwide Nitrogen Deposition
565 Monitoring Network (NNDMN) can be requested from Prof. Xuejun Liu in China
566 Agricultural University. The ground-based NH₃ measurements from the AMoN-US
567 can be downloaded from the website: <http://nadp.sws.uiuc.edu/AMoN/>. The
568 ground-based NH₃ measurements from the EMEP network can be gained from
569 <https://www.nilu.no/projects/ccc/emepdata.html>. The IASI-derived surface NH₃ used
570 in this study are available from the corresponding author upon request.

571

572 **Notes**

573 The authors declare that they have no conflict of interest.

574

575 **Reference**

576 Amos, H. M., Jacob, D. J., Holmes, C. D., Fisher, J. A., Wang, Q., Yantosca, R. M.,
577 Corbitt, E. S., Galarneau, E., Rutter, A. P., and Gustin, M. S.: Gas-particle partitioning
578 of atmospheric Hg(II) and its effect on global mercury deposition, *Atmospheric
579 Chemistry & Physics*, 11, 29441-29477, 2012.

580 Basto, S., Thompson, K., Phoenix, G., Sloan, V., Leake, J., and Rees, M.: Long-term
581 nitrogen deposition depletes grassland seed banks, *Nature Communication*, 6, 1-6,



582 10.1038/ncomms7185, 2015.

583 Dammers, E., Palm, M., Van Damme, M., Vigouroux, C., Smale, D., Conway, S.,
584 Toon, G. C., Jones, N., Nussbaumer, E., Warneke, T., Petri, C., Clarisse, L., Clerbaux,
585 C., Hermans, C., Lutsch, E., Strong, K., Hannigan, J. W., Nakajima, H., Morino, I.,
586 Herrera, B., Stremme, W., Grutter, M., Schaap, M., Wichink Kruit, R. J., Notholt, J.,
587 Coheur, P. F., and Erismann, J. W.: An evaluation of IASI-NH₃ with ground-based
588 Fourier transform infrared spectroscopy measurements, *Atmos. Chem. Phys.*, 16,
589 10351-10368, 10.5194/acp-16-10351-2016, 2016.

590 Dentener, F., Drevet, J., Lamarque, J., Bey, I., Eickhout, B., Fiore, A., Hauglustaine,
591 D., Horowitz, L., Krol, M., and Kulshrestha, U.: Nitrogen and sulfur deposition on
592 regional and global scales: a multimodel evaluation, *Global Biogeochemical Cycles*,
593 20, 2006.

594 E., P. K., L., J. R., and K., R. H.: Retrieval of NO₂ vertical profiles from
595 ground-based UV-visible measurements: Method and validation, *Journal of*
596 *Geophysical Research: Atmospheres*, 102, 19089-19097, doi:10.1029/97JD00603,
597 1997.

598 Eerden, L. J. M. V. D.: Toxicity of ammonia to plants, *Agriculture & Environment*, 7,
599 223-235, 1982.

600 Fountoukis, C., and Nenes, A.: ISORROPIA II: a computationally efficient
601 thermodynamic equilibrium model for
602 K⁺ 'CCa₂⁺ 'CMg₂⁺ 'CNH₄⁺ 'CNa⁺ 'CSO₄²⁻ 'CNO₃ 'CCl 'CH₂O aerosols,
603 *Atmospheric Chemistry and Physics (ACP) & Discussions (ACPD)*, 2007.

604 Geddes, J. A., Martin, R. V., Boys, B. L., and van Donkelaar, A.: Long-term trends
605 worldwide in ambient NO₂ concentrations inferred from satellite observations,
606 *Environmental Health Perspectives (Online)*, 124, 281, 2016.

607 Geng, G., Zhang, Q., Martin, R. V., Donkelaar, A. V., Huo, H., Che, H., Lin, J., and
608 He, K.: Estimating long-term PM 2.5 concentrations in China using satellite-based
609 aerosol optical depth and a chemical transport model, *Remote Sensing of*
610 *Environment*, 166, 262-270, 2015.

611 Giglio, L., Csiszar, I., and Justice, C. O.: Global distribution and seasonality of active



612 fires as observed with the Terra and Aqua Moderate Resolution Imaging
613 Spectroradiometer (MODIS) sensors, *Journal of Geophysical Research*
614 *Biogeosciences*, 111, 17-23, 2015.

615 Gilliland, A. B., Wyatt Appel, K., Pinder, R. W., and Dennis, R. L.: Seasonal NH₃
616 emissions for the continental united states: Inverse model estimation and evaluation,
617 *Atmospheric Environment*, 40, 4986-4998,
618 <https://doi.org/10.1016/j.atmosenv.2005.12.066>, 2006.

619 Graaf, S. C. v. d., Dammers, E., Schaap, M., and Erisman, J. W.: How are NH₃ dry
620 deposition estimates affected by combining the LOTOS-EUROS model with
621 IASI-NH₃ satellite observations?, *Atmospheric Chemistry and Physics Discussions*,
622 <https://doi.org/10.5194/acp-2018-133>, 2018.

623 Huang, X., Song, Y., Li, M., Li, J., Huo, Q., Cai, X., Zhu, T., Hu, M., and Zhang, H.:
624 A high resolution ammonia emission inventory in China, *Global Biogeochemical*
625 *Cycles*, 26, 1-14, 2012.

626 Kharol, S. K., Shephard, M. W., McLinden, C. A., Zhang, L., Sioris, C. E., O'Brien, J.
627 M., Vet, R., Cady-Pereira, K. E., Hare, E., Siemons, J., and Krotkov, N. A.: Dry
628 Deposition of Reactive Nitrogen From Satellite Observations of Ammonia and
629 Nitrogen Dioxide Over North America, *Geophysical Research Letters*, 45, 1157-1166,
630 [10.1002/2017GL075832](https://doi.org/10.1002/2017GL075832), 2018.

631 Kim, T. W., Lee, K., Duce, R., and Liss, P.: Impact of atmospheric nitrogen deposition
632 on phytoplankton productivity in the South China Sea, *Geophysical Research Letters*,
633 41, 3156–3162, 2014.

634 Lamarque, J. F., Kiehl, J., Brasseur, G., Butler, T., Cameron - Smith, P., Collins, W.,
635 Collins, W., Granier, C., Hauglustaine, D., and Hess, P.: Assessing future nitrogen
636 deposition and carbon cycle feedback using a multimodel approach: Analysis of
637 nitrogen deposition, *Journal of Geophysical Research: Atmospheres* (1984–2012), 110,
638 2005.

639 Lamsal, L. N., Martin, R. V., van Donkelaar, A., Steinbacher, M., Celarier, E. A.,
640 Bucsela, E., Dunlea, E. J., and Pinto, J. P.: Ground-level nitrogen dioxide
641 concentrations inferred from the satellite-borne Ozone Monitoring Instrument, *Journal*



642 of Geophysical Research: Atmospheres, 113, 1-15, 10.1029/2007JD009235, 2008.

643 Lamsal, L. N., Martin, R. V., Parrish, D. D., and Krotkov, N. A.: Scaling relationship
644 for NO₂ pollution and urban population size: a satellite perspective, Environmental
645 Science & Technology, 47, 7855-7861, 2013.

646 Larssen, T., Duan, L., and Mulder, J.: Deposition and leaching of sulfur, nitrogen and
647 calcium in four forested catchments in China: implications for acidification,
648 Environmental science & technology, 45, 1192-1198, 2011.

649 Levine, J. S., Augustsson, T. R., and Hoell, J. M.: The vertical distribution of
650 tropospheric ammonia, Geophysical Research Letters, 7, 317-320,
651 10.1029/GL007i005p00317, 1980.

652 Li, M., Zhang, Q., Kurokawa, J., Woo, J. H., He, K., Lu, Z., Ohara, T., Song, Y.,
653 Streets, D. G., and Carmichael, G. R.: MIX: a mosaic Asian anthropogenic emission
654 inventory under the international collaboration framework of the MICS-Asia and
655 HTAP, Atmospheric Chemistry & Physics, 17, 34813-34869, 2017a.

656 Li, Y., Schwandner, F. M., Sewell, H. J., Zivkovich, A., Tigges, M., Raja, S., Holcomb,
657 S., Molenaar, J. V., Sherman, L., and Archuleta, C.: Observations of ammonia, nitric
658 acid, and fine particles in a rural gas production region, Atmospheric Environment, 83,
659 80-89, 2014.

660 Li, Y., Schichtel, B. A., Walker, J. T., Schwede, D. B., Chen, X., Lehmann, C. M.,
661 Puchalski, M. A., Gay, D. A., and Collett, J. L.: Increasing importance of deposition of
662 reduced nitrogen in the United States, Proceedings of the National Academy of
663 Sciences, 113, 5874-5879, 2016.

664 Li, Y., Thompson, T. M., Damme, M. V., Chen, X., Benedict, K. B., Shao, Y., Day, D.,
665 Boris, A., Sullivan, A. P., and Ham, J.: Temporal and Spatial Variability of Ammonia
666 in Urban and Agricultural Regions of Northern Colorado, United States, Atmospheric
667 Chemistry & Physics, 17, 1-50, 2017b.

668 Lin, J. T., Martin, R. V., Boersma, K. F., Sneep, M., Stammes, P., Spurr, R., Wang, P.,
669 Van Roozendaal, M., Clémer, K., and Irie, H.: Retrieving tropospheric nitrogen
670 dioxide from the Ozone Monitoring Instrument: effects of aerosols, surface
671 reflectance anisotropy, and vertical profile of nitrogen dioxide, Atmos. Chem. Phys.,



672 14, 1441-1461, 10.5194/acp-14-1441-2014, 2014.

673 Liu, H., Jacob, D. J., Bey, I., and Yantosca, R. M.: Constraints from 210Pb and 7Be on
674 wet deposition and transport in a global three-dimensional chemical tracer model
675 driven by assimilated meteorological fields, *Journal of Geophysical Research:*
676 *Atmospheres*, 106, 12109-12128, 10.1029/2000JD900839, 2001.

677 Liu, L., Zhang, X., Xu, W., Liu, X., Li, Y., Lu, X., Zhang, Y., and Zhang, W.:
678 Temporal characteristics of atmospheric ammonia and nitrogen dioxide over China
679 based on emission data, satellite observations and atmospheric transport modeling
680 since 1980, *Atmospheric Chemistry & Physics*, 17, 1-32, 2017a.

681 Liu, L., Zhang, X., Xu, W., Liu, X., Lu, X., Wang, S., Zhang, W., and Zhao, L.:
682 Ground Ammonia Concentrations over China Derived from Satellite and Atmospheric
683 Transport Modeling, *Remote Sensing*, 9, 467, 2017b.

684 Liu, L., Zhang, X., Zhang, Y., Xu, W., Liu, X., Zhang, X., Feng, J., Chen, X., Zhang,
685 Y., Lu, X., Wang, S., Zhang, W., and Zhao, L.: Dry Particulate Nitrate Deposition in
686 China, *Environmental Science & Technology*, 10.1021/acs.est.7b00898, 2017c.

687 Liu, M., Huang, X., Song, Y., Xu, T., Wang, S., Wu, Z., Hu, M., Zhang, L., Zhang, Q.,
688 Pan, Y., Liu, X., and Zhu, T.: Rapid SO₂ emission reductions significantly increase
689 tropospheric ammonia concentrations over the North China Plain, *Atmos. Chem.*
690 *Phys.*, 18, 17933-17943, 10.5194/acp-18-17933-2018, 2018.

691 Mao, J., Paulot, F., Jacob, D. J., Cohen, R. C., Crouse, J. D., Wennberg, P. O., Keller,
692 C. A., Hudman, R. C., Barkley, M. P., and Horowitz, L. W.: Ozone and organic
693 nitrates over the eastern United States: Sensitivity to isoprene chemistry, *Journal of*
694 *Geophysical Research Atmospheres*, 118, 11-11,268, 2013.

695 Nowlan, C., Martin, R., Philip, S., Lamsal, L., Krotkov, N., Marais, E., Wang, S., and
696 Zhang, Q.: Global dry deposition of nitrogen dioxide and sulfur dioxide inferred from
697 space - based measurements, *Global Biogeochemical Cycles*, 28, 1025-1043, 2014.

698 Pan, Y., Tian, S., Zhao, Y., Zhang, L., Zhu, X., Gao, J., Huang, W., Zhou, Y., Song, Y.,
699 and Zhang, Q.: Identifying ammonia hotspots in China using a national observation
700 network, *Environmental Science & Technology*, 2018.

701 Paulot, F., Jacob, D. J., Pinder, R. W., Bash, J. O., Travis, K., and Henze, D. K.:



702 Ammonia emissions in the United States, European Union, and China derived by
703 high-resolution inversion of ammonium wet deposition data: Interpretation with a new
704 agricultural emissions inventory (MASAGE_NH3), *Journal of Geophysical Research:*
705 *Atmospheres*, 119, 4343-4364, 10.1002/2013JD021130, 2014.

706 Potter, P., Ramankutty, N., Bennett, E. M., and Donner, S. D.: Characterizing the
707 Spatial Patterns of Global Fertilizer Application and Manure Production, *Earth*
708 *Interactions*, 14, 1-22, 10.1175/2009EI288.1, 2010.

709 Pye, H. O. T., Liao, H., Wu, S., Mickley, L. J., Jacob, D. J., Henze, D. K., and
710 Seinfeld, J. H.: Effect of changes in climate and emissions on future
711 sulfate-nitrate-ammonium aerosol levels in the United States, *Journal of Geophysical*
712 *Research: Atmospheres*, 114, doi:10.1029/2008JD010701, 2009.

713 Reay, D. S., Dentener, F., Smith, P., Grace, J., and Feely, R. A.: Global nitrogen
714 deposition and carbon sinks, *Nature Geoscience*, 1, 430-437, 2008.

715 Richter, A., Burrows, J. P., Nüß, H., Granier, C., and Niemeier, U.: Increase in
716 tropospheric nitrogen dioxide over China observed from space, *Nature*, 437, 129-132,
717 2005.

718 Rozanov, A., Bovensmann, H., Bracher, A., Hrechanyy, S., Rozanov, V., Sinnhuber,
719 M., Strohm, F., and Burrows, J. P.: NO₂ and BrO vertical profile retrieval from
720 SCIAMACHY limb measurements: Sensitivity studies, *Advances in Space Research*,
721 36, 846-854, <https://doi.org/10.1016/j.asr.2005.03.013>, 2005.

722 Schaap, M., van Loon, M., ten Brink, H. M., Dentener, F. J., and Builtjes, P. J. H.:
723 Secondary inorganic aerosol simulations for Europe with special attention to nitrate,
724 *Atmos. Chem. Phys.*, 4, 857-874, 10.5194/acp-4-857-2004, 2004.

725 Schiferl, L. D., Heald, C. L., Nowak, J. B., Holloway, J. S., Neuman, J. A., Bahreini,
726 R., Pollack, I. B., Ryerson, T. B., Wiedinmyer, C., and Murphy, J. G.: An investigation
727 of ammonia and inorganic particulate matter in California during the CalNex
728 campaign, *Journal of Geophysical Research: Atmospheres*, 119, 1883-1902, 2014.

729 Schiferl, L. D., Heald, C. L., Van Damme, M., Pierrefrancois, C., and Clerbaux, C.:
730 Interannual Variability of Ammonia Concentrations over the United States: Sources
731 and Implications for Inorganic Particulate Matter, *Atmospheric Chemistry & Physics*,



- 732 1-42, 2015.
- 733 Shephard, M., and Cady-Pereira, K.: Cross-track Infrared Sounder (CrIS) satellite
734 observations of tropospheric ammonia, *Atmospheric Measurement Techniques*, 8,
735 1323-1336, 2015.
- 736 Shephard, M. W., Cady-Pereira, K. E., Luo, M., Henze, D. K., Pinder, R. W., Walker, J.
737 T., Rinsland, C. P., Bash, J. O., Zhu, L., Payne, V. H., and Clarisse, L.: TES ammonia
738 retrieval strategy and global observations of the spatial and seasonal variability of
739 ammonia, *Atmos. Chem. Phys.*, 11, 10743-10763, [10.5194/acp-11-10743-2011](https://doi.org/10.5194/acp-11-10743-2011), 2011.
- 740 Sheppard, L. J., Leith, I. D., Crossley, A., Dijk, N. V., Fowler, D., Sutton, M. A., and
741 Woods, C.: Stress responses of *Calluna vulgaris* to reduced and oxidised N applied
742 under 'real world conditions', *Environmental Pollution*, 154, 404-413, 2008.
- 743 Simon, H., Allen, D. T., and Wittig, A. E.: Fine particulate matter emissions
744 inventories: comparisons of emissions estimates with observations from recent field
745 programs, *Journal of the Air & Waste Management Association*, 58, 320-343, 2008.
- 746 Tørseth, K., Aas, W., Breivik, K., Fjæraa, A. M., Fiebig, M., Hjellbrekke, A. G., Lund
747 Myhre, C., Solberg, S., and Yttri, K. E.: Introduction to the European Monitoring and
748 Evaluation Programme (EMEP) and observed atmospheric composition change
749 during 1972–2009, *Atmospheric Chemistry & Physics*, 12, 5447-5481, 2012.
- 750 Tevlin, A. G., Li, Y., Collett, J. L., McDuffie, E. E., Fischer, E. V., and Murphy, J. G.:
751 Tall Tower Vertical Profiles and Diurnal Trends of Ammonia in the Colorado Front
752 Range, *Journal of Geophysical Research Atmospheres*, 122, 2017.
- 753 Van, D. A., Martin, R. V., Spurr, R. J., and Burnett, R. T.: High-Resolution
754 Satellite-Derived PM_{2.5} from Optimal Estimation and Geographically Weighted
755 Regression over North America, *Environmental Science & Technology*, 49,
756 10482-10491, 2015.
- 757 Van, D. A., Martin, R. V., Brauer, M., Hsu, N. C., Kahn, R. A., Levy, R. C., Lyapustin,
758 A., Sayer, A. M., and Winker, D. M.: Global Estimates of Fine Particulate Matter
759 using a Combined Geophysical-Statistical Method with Information from Satellites,
760 Models, and Monitors, *Environmental Science & Technology*, 50, 3762, 2016.
- 761 Van Damme, M., Clarisse, L., Dammers, E., Liu, X., Nowak, J., Clerbaux, C.,



762 Flechard, C., Galy-Lacaux, C., Xu, W., and Neuman, J.: Towards validation of
763 ammonia (NH₃) measurements from the IASI satellite, *Atmospheric Measurement*
764 *Techniques*, 7, 12125-12172, 2014a.

765 Van Damme, M., Clarisse, L., Heald, C., Hurtmans, D., Ngadi, Y., Clerbaux, C.,
766 Dolman, A., Erisman, J. W., and Coheur, P.-F.: Global distributions, time series and
767 error characterization of atmospheric ammonia (NH₃) from IASI satellite
768 observations, *Atmospheric Chemistry and Physics*, 14, 2905-2922, 2014b.

769 Van Damme, M., Wichink Kruit, R., Schaap, M., Clarisse, L., Clerbaux, C., Coheur, P.
770 F., Dammers, E., Dolman, A., and Erisman, J.: Evaluating 4 years of atmospheric
771 ammonia (NH₃) over Europe using IASI satellite observations and LOTOS - EUROS
772 model results, *Journal of Geophysical Research: Atmospheres*, 119, 9549-9566,
773 2014c.

774 Van Damme, M., Erisman, J. W., Clarisse, L., Dammers, E., Whitburn, S., Clerbaux,
775 C., Dolman, A. J., and Coheur, P. F.: Worldwide spatiotemporal atmospheric ammonia
776 (NH₃) columns variability revealed by satellite, *Geophysical Research Letters*, 42,
777 8660-8668, 2015.

778 Van Damme, M., Whitburn, S., Clarisse, L., Clerbaux, C., Hurtmans, D., and Coheur,
779 P. F.: Version 2 of the IASI NH₃ neural network retrieval algorithm: near-real-time and
780 reanalysed datasets, *Atmospheric Measurement Techniques*, 10, 1-14, 2017.

781 Van Damme, M., Clarisse, L., Whitburn, S., Hadji-Lazaro, J., Hurtmans, D., Clerbaux,
782 C., and Coheur, P.-F.: Industrial and agricultural ammonia point sources exposed,
783 *Nature*, 564, 99-103, 10.1038/s41586-018-0747-1, 2018.

784 Wang, Q., Jacob, D. J., Fisher, J. A., and Mao, J.: Sources of carbonaceous aerosols
785 and deposited black carbon in the Arctic in winter-spring: implications for radiative
786 forcing, *Atmospheric Chemistry & Physics Discussions*, 11, 19395-19442, 2011.

787 Wang, Y., Logan, J. A., and Jacob, D. J.: Global simulation of tropospheric O₃-NO_x
788 -hydrocarbon chemistry: 2. Model evaluation and global ozone budget, *Journal of*
789 *Geophysical Research Atmospheres*, 103, 10727-10755, 1998.

790 Warner, J. X., Wei, Z., Strow, L. L., Dickerson, R. R., and Nowak, J. B.: The global
791 tropospheric ammonia distribution as seen in the 13-year AIRS measurement record,



792 Atmospheric Chemistry and Physics, 16, 5467-5479, 2016.

793 Warner, J. X., Dickerson, R. R., Wei, Z., Strow, L. L., Wang, Y., and Liang, Q.:

794 Increased atmospheric ammonia over the world's major agricultural areas detected

795 from space, *Geophysical Research Letters*, n/a-n/a, 10.1002/2016GL072305, 2017.

796 Wesely, M.: Parameterization of surface resistances to gaseous dry deposition in

797 regional-scale numerical models, *Atmospheric Environment* (1967), 23, 1293-1304,

798 1989.

799 Whitburn, S., Van Damme, M., Kaiser, J. W., van der Werf, G. R., Turquety, S.,

800 Hurtmans, D., Clarisse, L., Clerbaux, C., and Coheur, P. F.: Ammonia emissions in

801 tropical biomass burning regions: Comparison between satellite-derived emissions

802 and bottom-up fire inventories, *Atmospheric Environment*, 121, 42-54,

803 <https://doi.org/10.1016/j.atmosenv.2015.03.015>, 2015.

804 Whitburn, S., Van Damme, M., Clarisse, L., Bauduin, S., Heald, C. L., Hadji-Lazaro,

805 J., Hurtmans, D., Zondlo, M. A., Clerbaux, C., and Coheur, P. F.: A flexible and robust

806 neural network IASI-NH₃ retrieval algorithm, *Journal of Geophysical Research:*

807 *Atmospheres*, 121, 6581-6599, 10.1002/2016JD024828, 2016.

808 Wiedinmyer, C., Akagi, S. K., Yokelson, R. J., Emmons, L. K., Alsaadi, J. A., Orlando,

809 J. J., and Soja, A. J.: The Fire INventory from NCAR (FINN): a high resolution global

810 model to estimate the emissions from open burning, *Geoscientific Model*

811 *Development*, 4, 3(2011-07-20), 3, 625-641, 2011.

812 Xia, Y., Zhao, Y., and Nielsen, C. P.: Benefits of China's efforts in gaseous pollutant

813 control indicated by the bottom-up emissions and satellite observations 2000–2014,

814 *Atmospheric Environment*, 136, 43-53,

815 <http://dx.doi.org/10.1016/j.atmosenv.2016.04.013>, 2016.

816 Xu, W., Luo, X. S., Pan, Y. P., Zhang, L., Tang, A. H., Shen, J. L., Zhang, Y., Li, K. H.,

817 Wu, Q. H., Yang, D. W., Zhang, Y. Y., Xue, J., Li, W. Q., Li, Q. Q., Tang, L., Lv, S. H.,

818 Liang, T., Tong, Y. A., Liu, P., Zhang, Q., Xiong, Z. Q., Shi, X. J., Wu, L. H., Shi, W.

819 Q., Tian, K., Zhong, X. H., Shi, K., Tang, Q. Y., Zhang, L. J., Huang, J. L., He, C. E.,

820 Kuang, F. H., Zhu, B., Liu, H., Jin, X., Xin, Y. J., SHi, X. K., Du, E. Z., Dore, A. J.,

821 Tang, S., Collett Jr, J. L., Goulding, K., Sun, Y. X., Ren, J., Zhang, F. S., and Liu, X. J.:



822 Quantifying atmospheric nitrogen deposition through a nationwide monitoring
823 network across China, *Atmospheric Chemistry and Physics*, 15, 12345-12360, 2015.

824 Xu, W., Song, W., Zhang, Y., Liu, X., Zhang, L., Zhao, Y., Liu, D., Tang, A., Yang, D.,
825 and Wang, D.: Air quality improvement in a megacity: implications from 2015 Beijing
826 Parade Blue pollution control actions, *Atmospheric Chemistry and Physics*, 17, 31-46,
827 2017.

828 Yu, Y., Xu, M., Yao, H., Yu, D., Qiao, Y., Sui, J., Liu, X., and Cao, Q.: Char
829 characteristics and particulate matter formation during Chinese bituminous coal
830 combustion, *Proceedings of the Combustion Institute*, 31, 1947-1954,
831 <http://dx.doi.org/10.1016/j.proci.2006.07.116>, 2007.

832 Zhang, L., Gong, S., Padro, J., and Barrie, L.: A size-segregated particle dry
833 deposition scheme for an atmospheric aerosol module, *Atmospheric Environment*, 35,
834 549-560, [http://dx.doi.org/10.1016/S1352-2310\(00\)00326-5](http://dx.doi.org/10.1016/S1352-2310(00)00326-5), 2001.

835 Zhang, L., Chen, Y., Zhao, Y., Henze, D. K., Zhu, L., Song, Y., Paulot, F., Liu, X., Pan,
836 Y., and Huang, B.: Agricultural ammonia emissions in China: reconciling bottom-up
837 and top-down estimates, *Atmospheric Chemistry & Physics*, 18, 1-36, 2017a.

838 Zhang, X., Wu, Y., Liu, X., Reis, S., Jin, J., Dragosits, U., Van Damme, M., Clarisse,
839 L., Whitburn, S., Coheur, P.-F., and Gu, B.: Ammonia Emissions May Be
840 Substantially Underestimated in China, *Environmental Science & Technology*, 51,
841 12089-12096, [10.1021/acs.est.7b02171](https://doi.org/10.1021/acs.est.7b02171), 2017b.

842 Zhang, Y., Mathur, R., Bash, J. O., Hogrefe, C., Xing, J., and Roselle, S. J.: Long-term
843 trends in total inorganic nitrogen and sulfur deposition in the U.S. from 1990 to 2010,
844 *Atmospheric Chemistry & Physics*, 1-27, 2018.

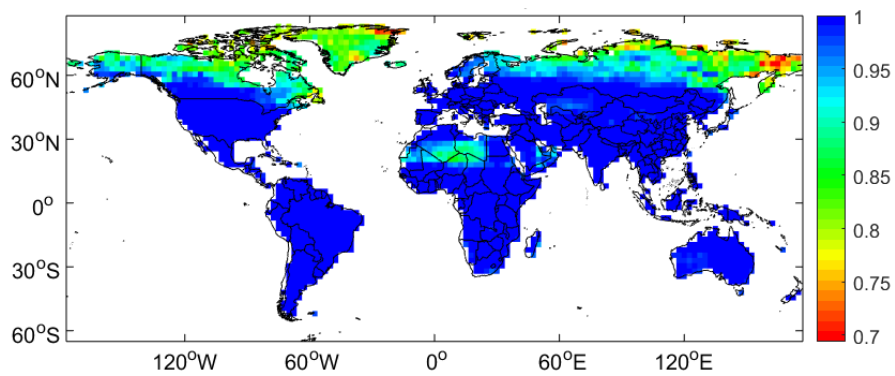
845 Zhu, L., Henze, D. K., Cady-Pereira, K. E., Shephard, M. W., Luo, M., Pinder, R. W.,
846 Bash, J. O., and Jeong, G. R.: Constraining U.S. ammonia emissions using TES
847 remote sensing observations and the GEOS - Chem adjoint model, *Journal of*
848 *Geophysical Research Atmospheres*, 118, 3355-3368, 2013.

849

850



851



852

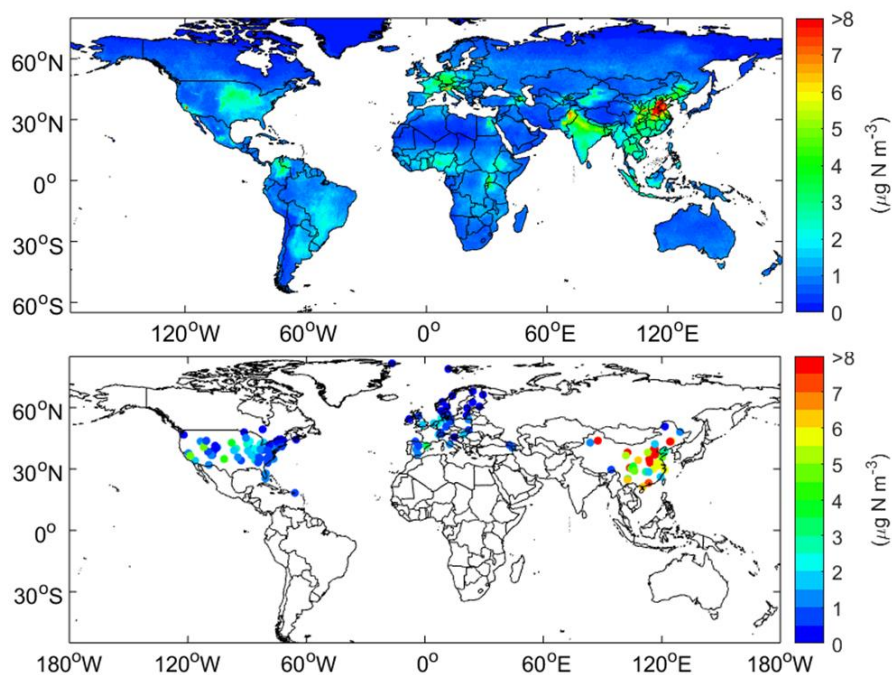
853

854

Fig. 1 R^2 of Gaussian fit for NH_3 vertical profiles.

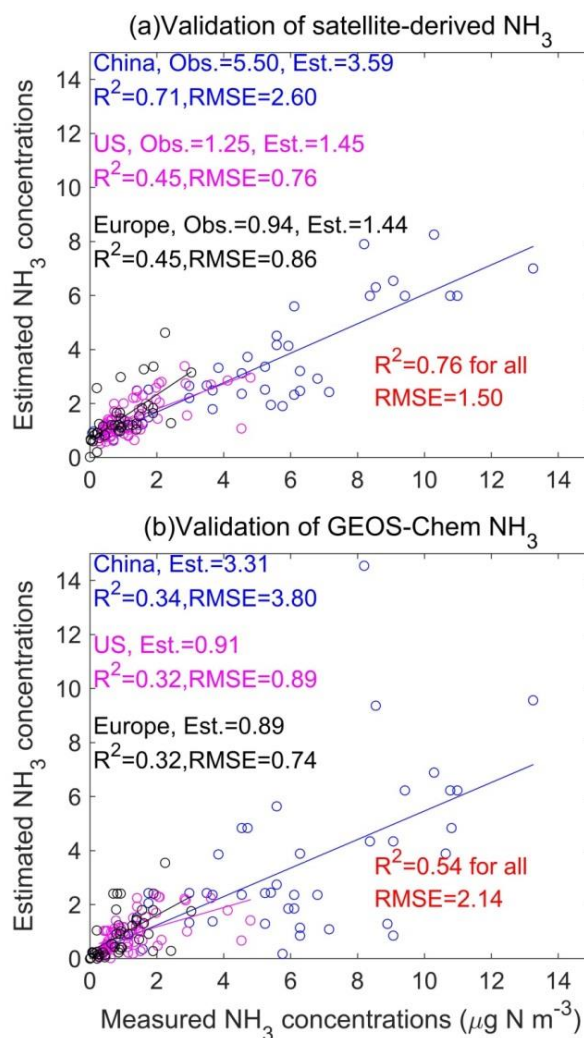


855



856
857

Fig. 2 Spatial distribution of satellite-derived and measured surface NH_3 concentrations in 2014.

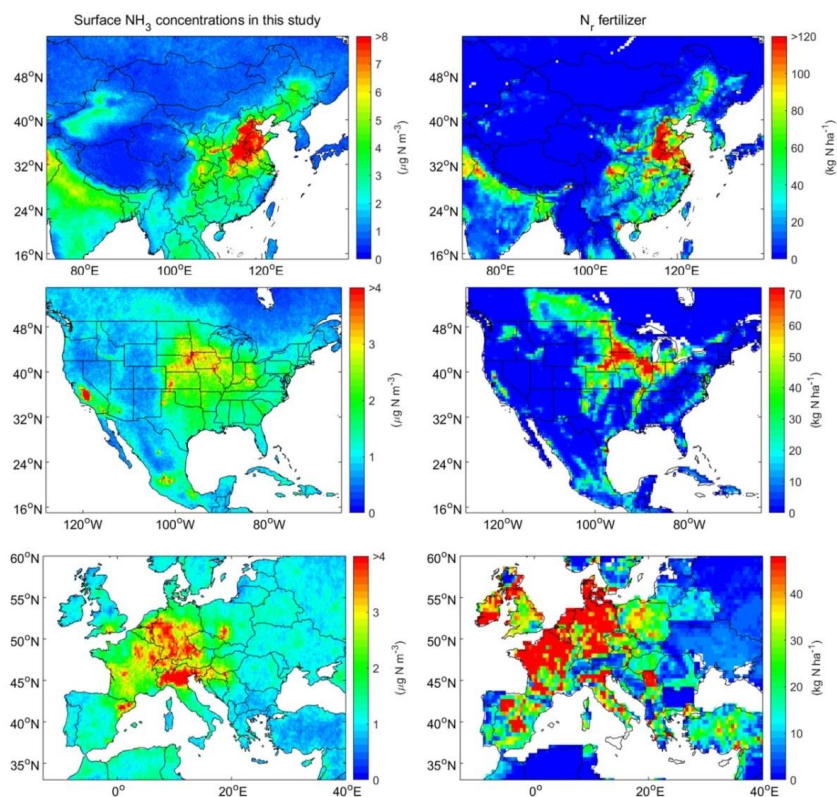


858

859

860

Fig. 3 Comparison of satellite-derived and GEOS-Chem modelled surface NH_3 concentrations with measured concentrations in China, US and Europe.



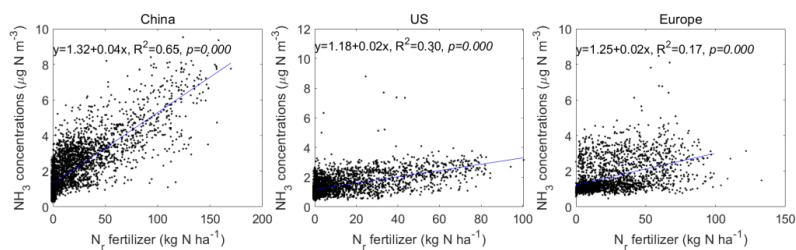
861

862 **Fig. 4** Spatial distribution of IASI-derived surface NH₃ concentrations and N fertilizer in China, Europe
863 and US.

864

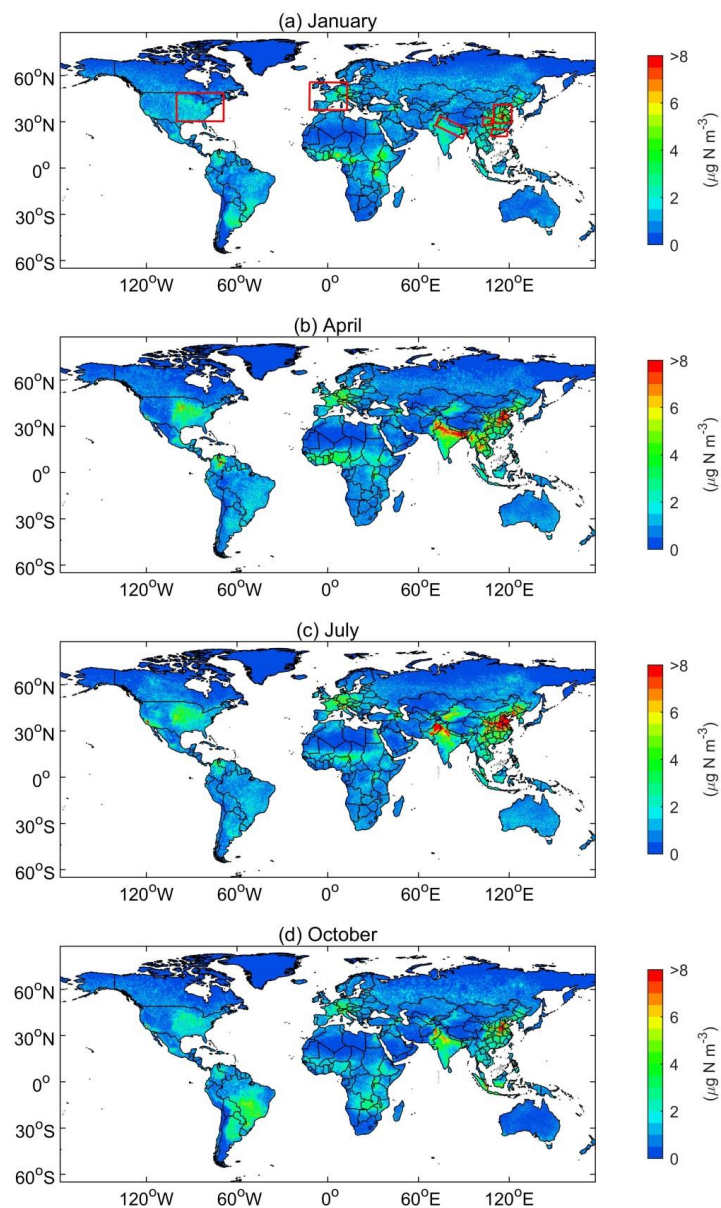


865



866

867 **Fig. 5** Comparison of satellite-derived surface NH_3 concentrations and N fertilizer amounts in China,
868 US and Europe. The spatial resolution of satellite-derived surface NH_3 concentrations and N fertilizer is
869 0.25° and 0.5° , respectively. We firstly resampled the satellite-derived surface NH_3 concentrations to
870 0.5° grids, and then compared it with N fertilizer data by each grid cell. We obtained the N fertilizer
871 data produced from McGill University (Potter et al., 2010).



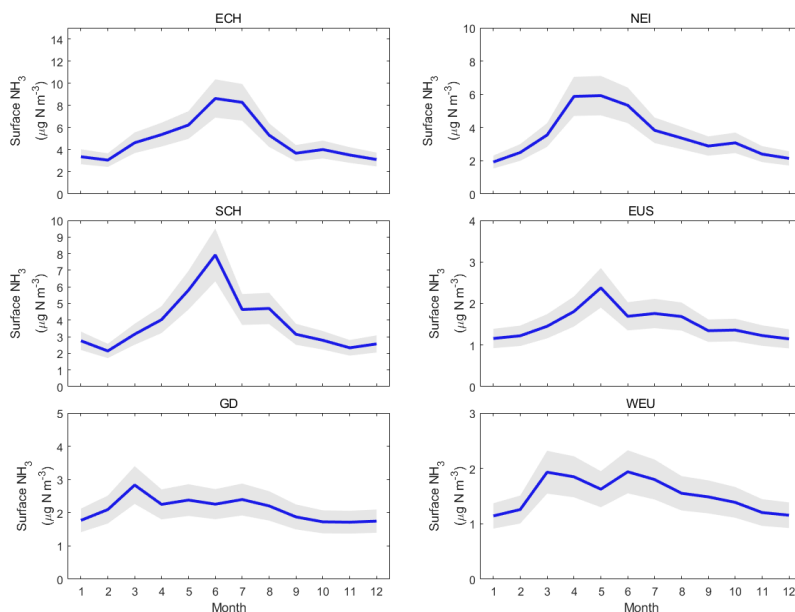
872

873

874

875

Fig. 6 Global surface NH₃ concentrations in January, April, July and October in 2014. The red rectangular regions include East China (ECH), Sichuan and Chongqing (SCH), Guangdong (GD), Northeast India (NEI), East US (EUS) and West Europe (WEU).

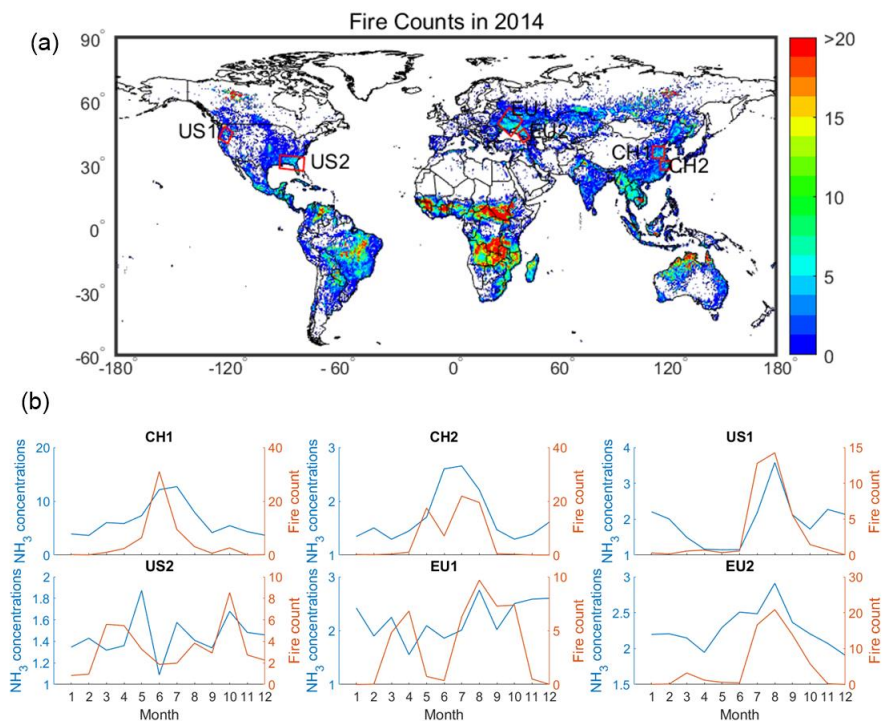


876

877 **Fig. 7** Monthly variations of surface NH_3 concentrations in hotspot regions including East China (ECH),
878 Sichuan and Chongqing (SCH), Guangdong (GD), Northeast India (NEI), East US (EUS) and West
879 Europe (WEU).
880



881



882

883

884

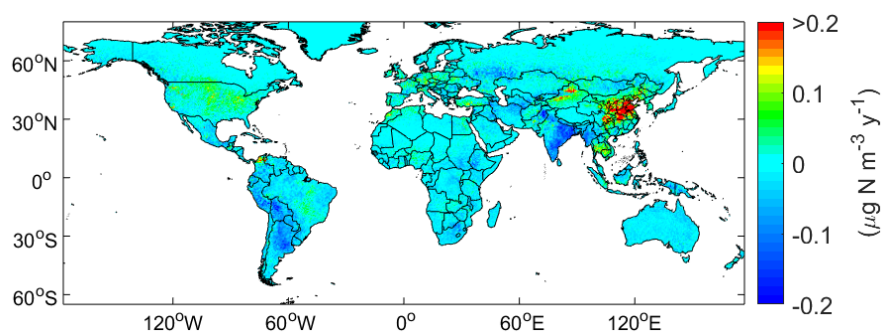
885

Fig. 8. Total raw fire count from the MODIS in 2014 (a), and monthly variations of fire counts and surface NH₃ concentrations in biomass burning regions in China, the US and Europe (b).



886

887



888

889 **Fig. 9** Trends of IASI-derived surface NH₃ concentrations between 2008 and 2016. A linear regression

890 was performed to calculate the trends. The significance value (p) and R² for the trends can be found in

891 **Fig. S10**.

892